Article

Single fibre enables acoustic fabrics via nanometre-scale vibrations

Check for updates

Wei Yan[1,2], Grace Noel[3], Gabriel Loke[1,2,13], Elizabeth Meiklejohn[4,13], Tural Khudiyev[1,13], Juliette Marion[2,13], Guanchun Rui[5], Jinuan Lin[6], Juliana Cherston[7], Atharva Sahasrabudhe[1,8], Joao Wilbert[7], Irmandy Wicaksono[7], Reed W. Hoyt[9], Anais Missakian[4], Lei Zhu[5], Chu Ma[6], John Joannopoulos[10,11] & Yoel Fink[1,2,12 ✉]

Fabrics, by virtue of their composition and structure, have traditionally been used as acoustic absorbers[1,2]. Here, inspired by the auditory system[3], we introduce a fabric that operates as a sensitive audible microphone while retaining the traditional qualities of fabrics, such as machine washability and draping. The fabric medium is composed of high-Young's modulus textile yarns in the weft of a cotton warp, converting tenuous 10^{-7}-atmosphere pressure waves at audible frequencies into lower-order mechanical vibration modes. Woven into the fabric is a thermally drawn composite piezoelectric fibre that conforms to the fabric and converts the mechanical vibrations into electrical signals. Key to the fibre sensitivity is an elastomeric cladding that concentrates the mechanical stress in a piezocomposite layer with a high piezoelectric charge coefficient of approximately 46 picocoulombs per newton, a result of the thermal drawing process. Concurrent measurements of electric output and spatial vibration patterns in response to audible acoustic excitation reveal that fabric vibrational modes with nanometre amplitude displacement are the source of the electrical output of the fibre. With the fibre subsuming less than 0.1% of the fabric by volume, a single fibre draw enables tens of square metres of fabric microphone. Three different applications exemplify the usefulness of this study: a woven shirt with dual acoustic fibres measures the precise direction of an acoustic impulse, bidirectional communications are established between two fabrics working as sound emitters and receivers, and a shirt auscultates cardiac sound signals.

The ubiquity of fabrics, together with recent breakthroughs in fibre technology, enable us to challenge traditional uses of fabrics to encompass new and potentially useful roles[4–8]. Fabrics have recently been shown to store energy[9], communicate[10], heat[11], cool[12,13], display[14] and even store and process digital information[15]. Motivated by the extent of fabric usage, its unparalleled proximity to the human body, and the importance of acoustic signals, we set out to investigate whether fabrics could serve as efficient sound collectors to detect and process even faint audible signals. The consequences of such a transformation in fabric use would be far-reaching—enabling fabrics to mediate acoustic communications, pick up acoustic health indicators from the body, and increase situational acoustic awareness.

Achieving sensitive acoustic fabrics faces two major obstacles. First, traditional fabrics are notorious for damping sound, and second, previously reported fibres capable of converting mechanical vibrations into electrical signals suffer from low sensitivity in air[16,17]. Fabrics are hierarchical constructs made of staple or filament fibres that are twisted into yarns and then assembled into fabrics. This hierarchy inherently establishes multiple interfaces, which scatter and dissipate propagating phonons, giving fabrics dissipative acoustic characteristics. In nature, however, fibres often serve the purpose of transmitting sounds instead of damping them. For example, in the human auditory system (Fig. 1), the tympanic membrane is responsible for resolving the acoustic impedance mismatch between the air of the ear canal and the fluid of the inner ear and happens to be a construct of high-modulus fibres oriented circumferentially and radially[18]. This membrane transduces sound pressure to mechanical vibrations of the middle ear bones. Such vibrations are then transmitted to the cochlea of the inner ear. In the cochlea, hair bundles are deflected to ultimately convert pressure waves into electrical signals (ionic) that are picked up by the nervous
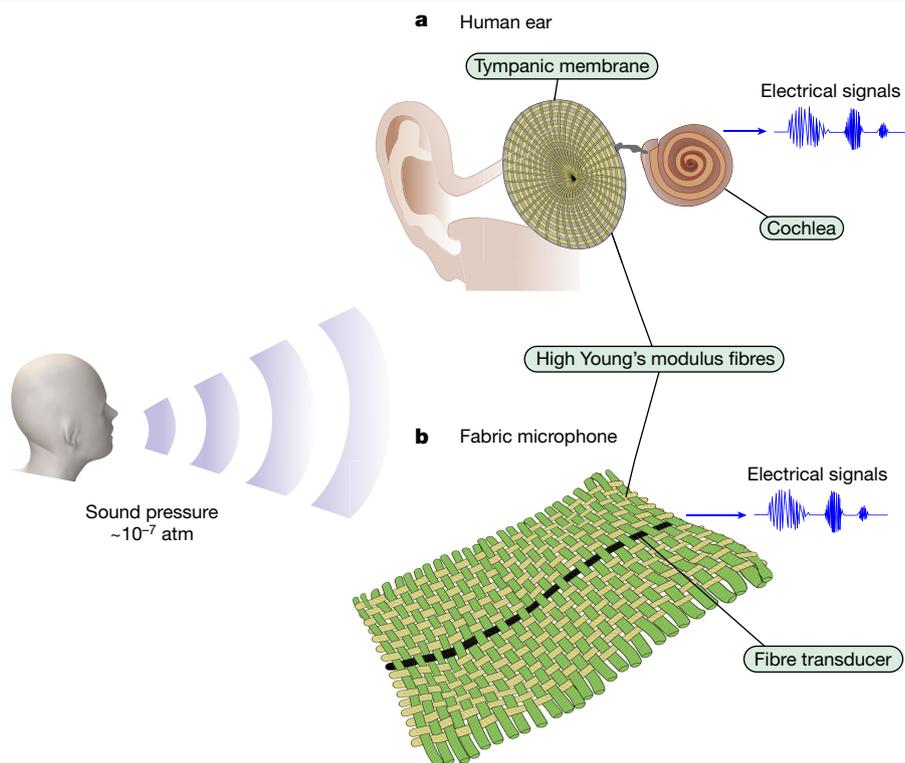
Fig. 1 | Design and principles of fabric microphones. a, The tympanic membrane is a four-layer construct composed of circumferentially and radially oriented high-modulus collagen fibres, which are key for sound conduction. The tympanic membrane motion is ultimately transmitted to the cochlea through the ossicular chain, wherein short cilia fibres convert pressure waves into electrical signals (ionic), which are picked up by the nervous system. **b**, In the acoustic fabric, high-modulus Twaron yarns and cotton yarns are oriented at right angles, mimicking the construction of the tympanic membrane. This construction converts faint audible frequency sound pressure waves into low-order mechanical vibration modes. Within that same medium, a single strand of piezoelectric elastomeric fibre transducer is woven, leading to a synergistically coupled fabric, where sound transduction is a collective effect. This results in a fabric capable of operating as a sensitive microphone that detects weak sound signals (for example, human speech) as low as 10^{-7} atm.

system[3]. Drawing inspiration from the auditory transduction sequence involving conversion of pressure to mechanical to electrical excitations and the importance of fibres in the auditory system, we introduce an approach with a similar transduction path that harnesses fibres to enable a minimally perturbed fabric to efficiently convert pressure waves to electrical output (Fig. 1).

Unlike the complex three-dimensional (3D) auditory system, we seek to achieve this conversion in a planar fabric. The fabric medium will play the part of the tympanic membrane to convert pressure waves into mechanical vibrations of a membrane. Woven into the fabric, the fibre transducer will have a similar role to the cochlea in providing electrical output. Given the conformal nature of the fibre, effective coupling, which is necessary for efficient conversion, occurs between the fabric and the fibre to form an acoustic fabric. Using a uniform membrane as a model for the eventual fabric medium, we begin with constructing a piezoelectric fibre that efficiently converts the membrane's vibrations into electrical output. We then employ laser vibrometry with concurrent electrical measurements to study the displacement modes of the membrane and fibre and elucidate the conversion mechanism. This guides the design of the woven acoustic fabrics, which detect nanometre displacement generated by audible acoustic waves, producing coherent electrical signals.

Fibre design and fabrication

Figure 2a outlines the piezoelectric fibre design and fabrication. The process begins with the construction of a macroscopic preform. The active layer is a composite consisting of piezoelectric poly(vinylidene fluoride-trifluoroethylene) (P(VDF-TrFE)) loaded with piezoelectric barium titanate (BaTiO$_3$) ceramic particles (Extended Data Fig. 1). P(VDF-TrFE) has a melting point of 150 °C (Extended Data Fig. 2), making it suitable for co-drawing with the other fibre materials. The high viscosity of carbon-loaded polyethylene (CPE) at the draw temperature delays the onset of capillary instability of the low-viscosity crystalline piezoelectric domain. During the draw, four copper wires are fed into the empty channels of the CPE, which in concert deliver excellent conductivity across two length scales—the microscale cross-section and the metre-scale fibre length. The innermost layers are asymmetrically encapsulated within an elastic poly (styrene-b-(ethylene-co-butylene)-b-styrene) (SEBS) cladding[19] (Fig. 2a; see Methods).

The preform is then thermally drawn into tens of metres of a fibre with submillimetre features. At the high voltages required by the poling process, small deviations in the thickness of the piezoelectric layer can lead to breakdown of the composite[20]. The required level of precise dimensional control is demonstrated by the production of a highly uniform 40-m-long fibre (Fig. 2b). The stable flow of all the materials preserves the cross-section geometry from the preform to the fibre. The interfaces between the P(VDF-TrFE)/BaTiO$_3$ and the CPE electrodes formed during the draw exhibit good adhesion (Fig. 2e, f). The nanoparticles maintain their homogenous distribution during the viscous flow (Fig. 2g). The thermal drawing process aligns the polymer chains along the draw direction (Extended Data Fig. 1c). The BaTiO$_3$ nanoparticles maintain their monocrystalline
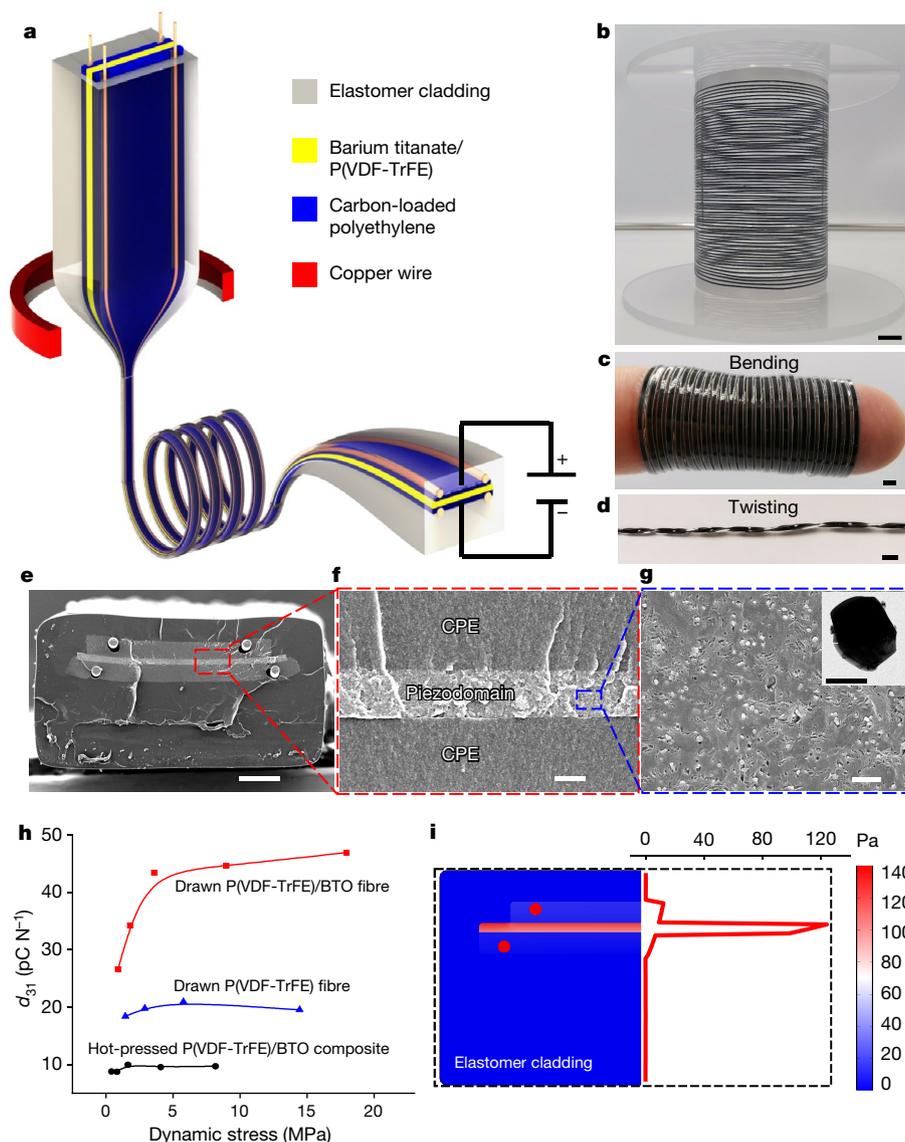
Fig. 2 | Acoustic fibre fabrication and characterization. a, Schematic of preform-to-fibre thermal drawing and fibre poling. **b**, Photograph of some portions of the 40-m-long fibre wrapped on a spool. **c**, Photograph of a piece of fibre wrapped on a finger, showing its high flexibility. **d**, Photograph of a piece of fibre twisted with an angle >540°. **e**, Scanning electron microscopy (SEM) micrograph of the fibre cross-section, showing that the fibre geometry is preserved after thermal drawing of the macroscopic preform. The gaps between the copper wires and the surrounding CPE electrodes were created during the cleaving process. **f**, High-resolution SEM micrograph showing the close interface between the CPE electrodes and the piezocomposite. **g**, High-resolution SEM micrograph showing the homogenous distribution of BaTiO₃ nanoparticles in the P(VDF-TrFE) matrix. **h**, Measured d_{31} piezoelectric coefficients of the hot-pressed composite, drawn P(VDF-TrFE) fibre, and drawn P(VDF-TrFE)/BaTiO₃ fibre. **i**, Simulated von Mises stress distribution in the cross-section of the fibre cladded by the SEBS cladding at 290 Hz. The left side shows the von Mises stress distribution using the color scale. The right side is a plot of the von Mises stress down the center of the cross-section. Higher stress leads to higher output voltage for the piezocomposite (which is the red layer showing high stress). In addition to the piezocomposite layer, the other red regions experiencing high stress are the copper wires. More details about the simulation are given in Methods and Supplementary Note 8. Scale bars, 2 cm (**b**), 2 mm (**c**, **d**), 200 µm (**e**), 20 µm (**f**), 2 µm (**g**), 200 nm (**g**, inset).

tetragonal phase (Extended Data Fig. 1d), and the introduction of nanoparticles into the P(VDF-TrFE) does not deteriorate its flexibility (Supplementary Fig. 5).

The fibre loaded with 20 wt% BaTiO₃ nanoparticles exhibits substantially improved ferroelectric properties with a remanent polarization as high as 10 µC cm⁻² (Extended Data Fig. 2a). To achieve a highly sensitive sound transducer, we develop a stepwise poling method to align the dipoles in the piezocomposite (Extended Data Fig. 2b). Alternating the increasing applied voltage with 0-V relaxation periods not only mitigates the risk of dielectric breakdown during the poling process but also endows the composite with excellent piezoelectric properties[21]. We measured the piezoelectric charge coefficient d_{31} to be as high as

approximately 46 pC N⁻¹, considerably higher than that of the drawn P(VDF-TrFE) fibre (about 20 pC N⁻¹) and that of the hot-pressed P(VDF-TrFE)/BaTiO₃ composite (approximately 10 pC N⁻¹; Fig. 2h), as well as superior to existing PVDF-based piezoelectric materials (Extended Data Table 1). Microscopic analysis identifies voids around the BaTiO₃ particles observed only in the drawn fibre, suggesting the existence of a porous ferroelectret structure due to cavitation[22] between the BaTiO₃ particles and the P(VDF-TrFE) matrix. This structure can provide one explanation for the comparatively high d_{31} observed only in the drawn fibre (Supplementary Note 2).

The use of the elastomeric thermoplastic as the fibre cladding is motivated by many considerations. First, the combination of this
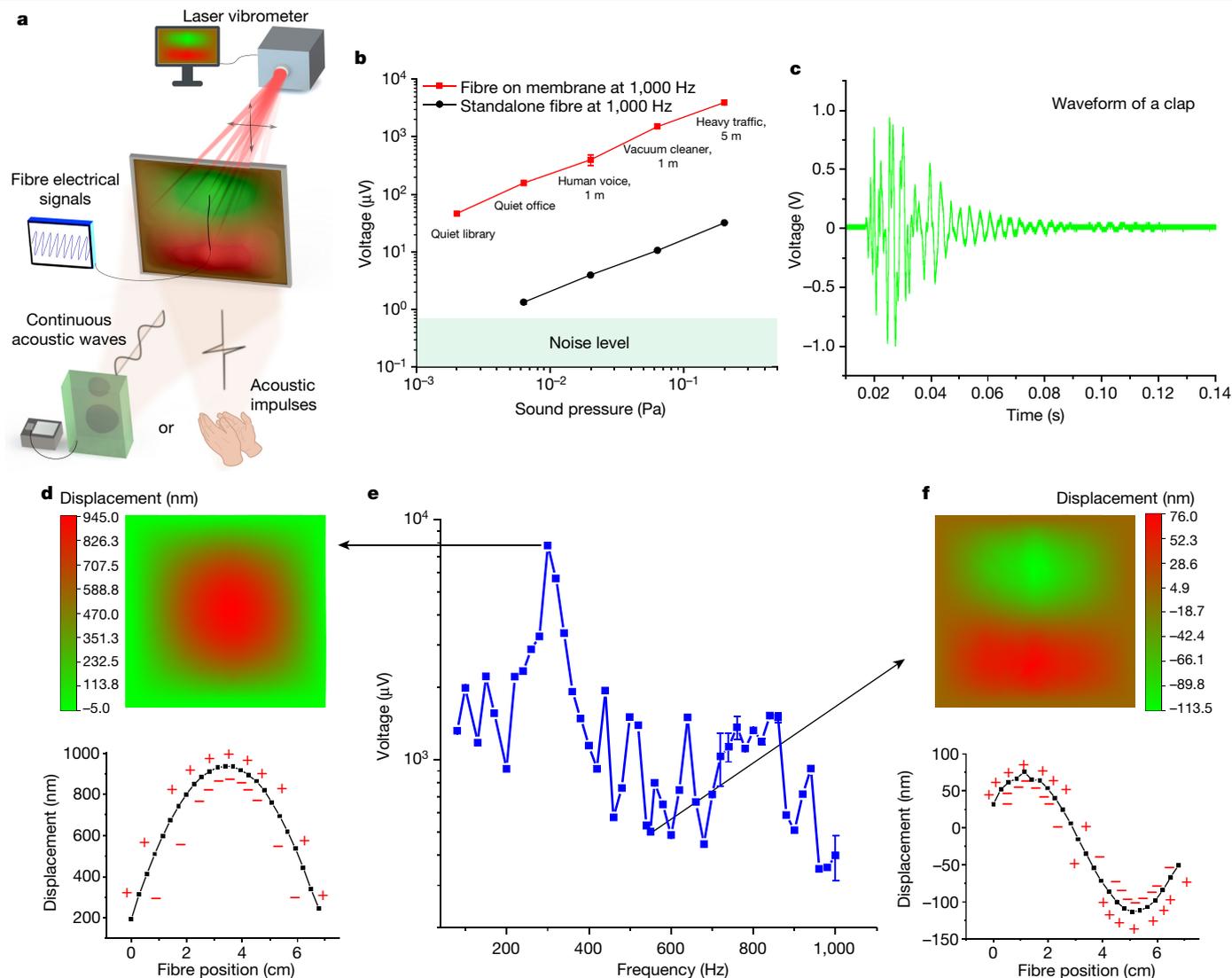
Fig. 3 | Acoustic fibre-on-membrane characterization. a, The schematic shows the concurrent measurement. The continuous sound waves are generated from a speaker and the impulse is generated from a clap. The vibration modes of the membrane under the impact of the continuous sound waves generated from the speaker are measured. **b**, The output voltage versus sound pressure of the fibre-on-Mylar system at 1,000 Hz. The performance of the standalone fibre is presented for a comparison. The noise level is also shown. **c**, The output voltage of the fibre-on-Mylar system in response to a clap. (Note that this is the voltage after it has been amplified 68×.) **d**, Measured vibrational (1, 1) modes together with z displacement (perpendicular to membrane surface) of the membrane (top) and fibre (bottom) at a resonance frequency of 300 Hz. **e**, Measured frequency response of the sample from 80 to 1,000 Hz. **f**, Measured vibrational (1, 2) modes together with z displacement (perpendicular to membrane surface) of the membrane (top) and fibre (bottom) at an anti-resonance frequency of 550 Hz. Because the laser vibrometer reads the back side of the membrane, we infer the fibre displacement by measuring the membrane displacement behind it. The positive and negative signs on the displacement curves (**d**, **f**, bottom) represent generated charges. Locations with higher curvatures have higher charge densities. The fibre is located vertically in the centre of the membrane (8 cm by 8 cm). The voltage measurements were repeated three times. After the first measurement, the fibre was removed from the sample and reattached for the next measurement. The error is the standard deviation of the three measurements.

elastomeric cladding with the stiffer piezoelectric composite results in stress concentration in the active piezoelectric domain (Fig. 2i and Supplementary Fig. 12). Second, the low modulus of the SEBS cladding contributes to the fibre bending compliance, an important aspect when designing a fibre that needs to conformally match to membrane vibration modes. The flexibility is also key to machine weaving into fabrics. Lastly, SEBS possesses excellent rheological properties (Extended Data Fig. 3), enabling preservation of the cross-sectional geometry of the resulting fibre. Owing to the low Young's modulus (3.79 MPa, Supplementary Fig. 13), the fibre tolerates some sophisticated deformations such as bending and twisting (Fig. 2c, d). Its capacitance remains stable over 3,000 cycles of bending or twisting (Extended Data Fig. 4). The ten machine-washing tests further demonstrate its high reliability and mechanical compliance. (Supplementary Fig. 14).

Fibre-on-membrane model

Once drawn and poled, the standalone piezoelectric fibre responds to acoustic waves in the audible range (Fig. 3a). When the fibre is mounted on a Mylar membrane, the electrical output is considerably larger. The boundary condition of the membrane should be well controlled via clamping and tensioning to achieve reproducible, reliable results (Supplementary Note 5). The output voltage of the fibre-on-membrane

Fig. 4 | Fabrication and characterization of woven acoustic fabrics. a, The fibre with a length of approximately 70 m is incorporated into the fabric during the weaving process. Note that the scale bar applies to the fabric, and the fibre on the spool is closer to the camera to better exhibit the fibre. **b**, A photograph of the Twaron-weft acoustic fibre containing one fibre transducer (6.7 cm in length) woven in the weft. **c**, The fabric was fixed in a frame (8 cm by 8 cm) with well controlled boundary conditions (Supplementary Note 5) for acoustic characterization. Measured frequency response of the fabric sample (8 cm by 8 cm). The schematics of the Twaron/cotton fabric (right) and the cotton fabric (left) are also shown. Warp yarns are shown horizontally and weft yarns are shown vertically. **d**, Measured vibrational modes together with z displacement (perpendicular to membrane surface) of the two fabrics and fibres at their resonance and anti-resonance frequencies using the laser vibrometer. The measurements for cotton at 240 Hz and 460 Hz are shown at top left and bottom left, respectively, and the measurements for Twaron/cotton at 230 Hz and 320 Hz are shown at top right and bottom right, respectively. Scale bars, 5 cm (**a**), 1 cm (**b**).

is measured in response to continuous waves generated by a speaker in the audible range under a sound pressure level of 60 dB (approximately 10^{-7} atm) or at a fixed frequency under different sound pressure levels.

The strong coupling between the fibre and the membrane mechanical vibration modes produces an electrical output that is two orders of magnitude higher than that of the standalone fibre (Fig. 3b). The

output voltage (several orders of magnitude higher than the noise level) increases linearly with increasing sound pressure level, consistent with the typical acoustic response of linear materials[23]. The minimum sound-detection capability is 0.002 Pa (40 dB, the sound pressure level in a quiet library), outperforming many other thin-film-based acoustic sensors[24–26]. The high Young's modulus membrane experiences minimal losses, allowing the system to efficiently record a short impulse with high fidelity (Fig. 3c), as elaborated on in the next section.

A sensitivity of 19.6 mV (at 94 dB and 1 kHz, following standards in the field) of the fibre-on-membrane is measured, which is comparable to that of off-the-shelf condenser and dynamic microphones (Supplementary Table 3). The high sensitivity allows it to efficiently detect audible sounds, as demonstrated by the high signal-to-noise ratio of the measured voltage output when the system is subject to a wide range of sound sources, such as human speech, air blowing, leaves rustling and birds chirping (Supplementary Video 1 and Extended Data Fig. 5).

Transduction mechanism

To reveal the transduction mechanism of the fibre woven into the fabric, we begin by examining the simpler model of fibre-on-membrane described above. A speaker illuminates the fibre-on-membrane with audible acoustic waves (Fig. 3a). A scanning laser vibrometer measures the vibration of the membrane as a displacement map at various frequencies. Meanwhile, we measure the output voltage from the fibre. These simultaneous measurements allow us to correlate the electrical output from the fibre with the mechanical vibration modes of the membrane. The output voltage versus frequency in Fig. 3e shows a large peak of 8 mV at 300 Hz, followed by peaks of decreasing amplitude as the frequency increases. At 550 Hz, for example, the electrical output is 0.5 mV. Displacement maps reveal that at 300 Hz the membrane displays a low-order symmetric resonant vibration mode with large amplitude of approximately 950 nm (Fig. 3d), whereas at 550 Hz, the mode is antisymmetric and has a much smaller amplitude of about 110 nm (Fig. 3f).

A 3D acoustical-mechano-electro model (COMSOL Multiphysics) is developed to gain insights into the fibre-on-membrane using sinusoidal plane acoustic waves as the input and the electrical signal from the fibre as the output. The simulation results reveal that the dominant factor determining the fibre electrical output is its axial bending (Extended Data Fig. 6), which occurs when the fibre is conformally displaced by the membrane vibration modes.

Our measurements and simulations (and the Euler–Bernoulli beam theory, see Supplementary Note 7) reveal two main factors influencing the magnitude of the electrical output of the system. First, larger membrane displacement amplitudes associated with lower-order resonances result in a larger curvature of the fibre and thus more strain in the piezocomposite. Second, the curvature integral along the fibre length is correlated to the electrical output of the fibre. When the fibre curvature has the same sign along its length, the piezoelectric layer is subject to similar stress conditions (either tensile or compressive) and charges of the same type (either positive or negative) build up additively on the electrodes, leading to a high output voltage (Fig. 3d). When the curvature changes sign along the fibre length, the piezoelectric layer undergoes tensile and compressive stress at different locations, resulting in charge cancellation that reduces the output voltage (Fig. 3f). The curvature changes signs more rapidly along the fibre in higher-order modes, resulting in lower output voltage.

The simulations do not account for damping or modulus dispersion. It is reasonable, however, to expect that the overall decrease in performance with frequency is due to the higher damping of the mechanical vibrations of the membrane at higher frequencies[27] and the stiffening of the SEBS at higher frequencies leading to larger resistance to deformation.

The fibre displacement and its curvature are influenced by the geometrical (shape, size, thickness, boundary conditions, and so on) and
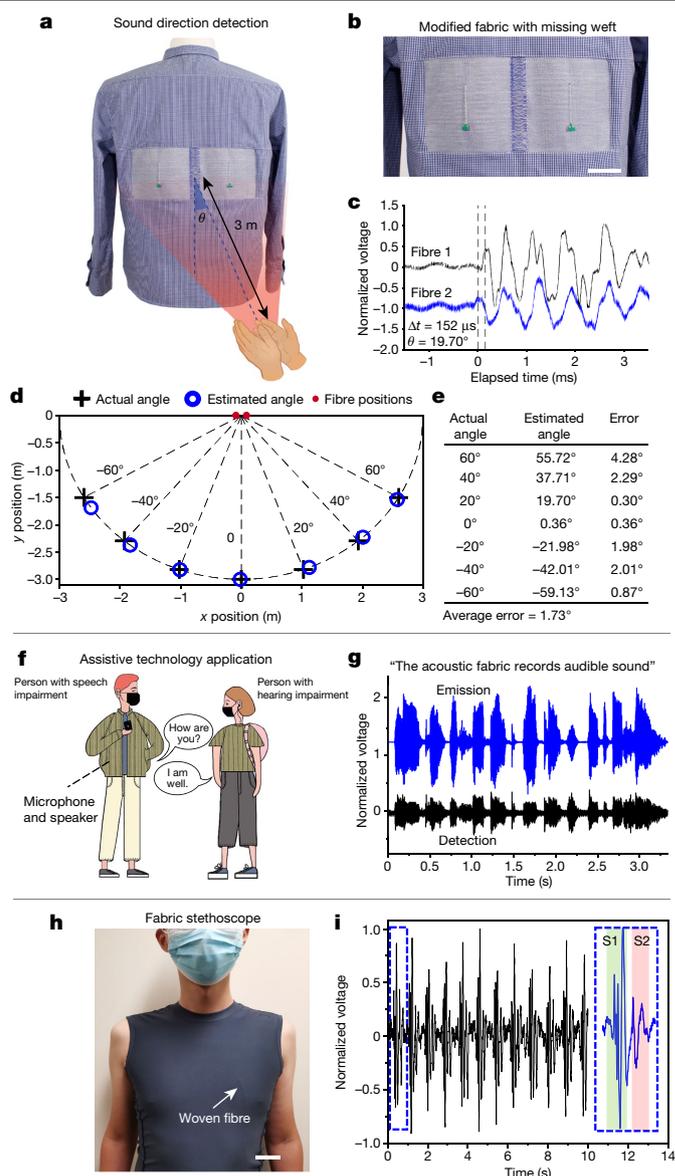

Fig. 5 | Examples of applications of the woven acoustic fabric integrated into shirts. a, Sound-direction detection. A shirt containing two fibres separated by some distance is used to detect the direction of the sound source. **b**, The fabric is modified by removing a section of the weft yarns to acoustically insulate the two fibres. **c**, The time difference between the peaks of the signal curve results in an estimated angle of 19.7°, which is 0.3° from the measured angle of 20°. **d, e**, Angles from −60° to 60° were tested with a clap at a distance of 3 m, and the mean error was 1.73°. At an angle greater than 60°, the impact of the sound waves on the fabric is reduced, making the peak detection difficult if the distance of the clap remains at 3 m. Schematic diagram (**d**) and measurement data (**e**) are shown. **f**, Acoustic communication application. Acoustic fabrics could act as an assistive technology that enables communication. **g**, Demonstration of acoustic communication using two shirts: one serves as a microphone and the other works as a speaker. The speech "The acoustic fabric records audible sound" emitted by one shirt is recorded by the other shirt (Supplementary Video 3). **h**, Fabric stethoscope application. Photograph of the experimental scenario. **i**, The shirt interfaces with the chest and can detect heart sounds, thus providing information about the cardiovascular system: it measures the heart rate and both the S1 and S2 components of the heart sound. For all measurements, the participants gave their informed consent to participate in the study and have their images and data published. Scale bars, 5 cm (**b, h**).

Article

mechanical properties (density, Young's modulus, Poisson's ratio, and so on) of the membrane. One can, however, heuristically conclude that when the vibration half-wavelength of the fibre matches the size of the membrane the signal is maximal. This is achieved by selecting a membrane that has a high modulus, resulting in fewer oscillations per unit membrane length, lower-order resonances[27], and thus large electrical output.

Woven acoustic fabric fabrication and characterization

Armed with these insights into the mechanism of transduction, we proceed to explore fabric designs optimized for acoustic collection and conversion. We construct two plain weave fabrics with different Young's moduli using a conventional weaving loom (Fig. 4a). The first fabric consists of cotton yarns in both the warp and the weft directions (Fig. 4c). This fabric has a lower modulus and is constructed of staple yarns. The second fabric has the same cotton warp but high-modulus Twaron filament yarns in the weft direction (Fig. 4b, c). The two fabrics have the same thickness, weight and dimensions, but differ in their moduli and the use of filament versus staple. The fibre transducer is woven into the fabrics. The tension of the warp cotton yarns that cross over the acoustic fibre is well controlled so that the fibre is not severely compressed. The fabric samples are then mounted on a frame with well controlled boundary conditions (Supplementary Fig. 18). The frequency response characterization reveals that the Twaron-weft fabric outperforms the cotton fabric (Fig. 4c). Note that the fabrics show excellent electrical signals at audible frequencies regardless of the specifics of tension or boundary conditions (Extended Data Fig. 7 and Supplementary Video 2).

The vibrational behaviour of the two fabrics at some representative frequencies is summarized in Fig. 4d, which reveals that nanometre displacement generated by audible acoustic waves can be efficiently detected and amplified in fabrics forming coherent electrical detection of sound. The anisotropic vibrational wavelength (longer wavelength on the weft and shorter wavelength on the warp) of the Twaron/cotton fabric and the isotropic vibrational wavelength (identical wavelength on both the weft and the warp) of the cotton fabric are notably revealed. At 230 Hz, a resonance frequency of the Twaron/cotton fabric, the modes of the fabric are of lower order and longer wavelength compared to those of the pure cotton fabric at 240 Hz. Shown also is the fibre displacement for these two fabrics, in which the curvature all has the same sign for the Twaron/cotton case, whereas it changes sign for the cotton. Similarly, owing to the lower-order modes of the Twaron/cotton fabric at the anti-resonance frequency of 320 Hz compared to those of the cotton fabric at 460 Hz, the bending wavelength of the fibre in the Twaron/cotton is much longer than that in the cotton. The electrical output for bending modes involves integration over the curvature function, which, when changing signs, leads to a cancellation effect and a diminishing output.

The magnitude of the fibre output depends on the order of the mode, its wavelength, and the fabric dimensions, which together yield different curvature integrals and electrical outputs. The sensitivity of the two-dimensional fabric microphone reaches 8 mV, attributed both to the high modulus and also to the lower losses associated with continuous filament, which compares well with many commercialized condenser and dynamic point microphones (Supplementary Table 3), demonstrating that indeed, fabrics can function as efficient sound collectors and transducers in the audible frequency range.

The scalability of the thermal drawing approach is well matched with the scale of industrial weaving processes (Fig. 4a). A typical acoustic fabric (36 cm × 23 cm) shown in Supplementary Video 2 only contains approximately 6.7 cm of fibre, which occupies around 0.1% of the volume of the fabric (Methods). In our study, 40 m of fibre is drawn from a preform in a single draw. This length can produce nearly 50 m^2 of acoustic fabric. The fabric maintains its electrical properties and acoustic sensitivity after ten machine-wash cycles (Extended Data Fig. 8).

Exemplary applications

The performance and form factor of the acoustic fibres enable a wide range of applications (Fig. 5). Here, the woven Twaron/cotton fabric is integrated into shirts. All the shirts are in a flexurally slack, draped condition (Supplementary Video 2). In Fig. 5a, b, the direction of an impulse is discerned by a shirt containing two fibres. A hand clap is initiated at various angles and the output from each fibre is recorded. The time delay between the peaks corresponds to a difference in the path length to the individual fibres (Fig. 5c), allowing for precise derivation of the direction of the clap (Fig. 5d, e). Directional detection could be useful for individuals with hearing aids to listen in specific directions while removing background noise, and for law enforcement seeking to detect a source of a gunshot. In addition to sensing sound, the fabric can also broadcast audible sounds when a modulated a.c. voltage is provided. As illustrated in Fig. 5f, Extended Data Fig. 9 and Supplementary Video 3, two shirts enable bidirectional acoustic communication with matched time-domain waveforms (Fig. 5g) and frequency-domain spectrograms between the emitted speech and the received speech, facilitating acoustic communication between individuals, which may be useful for people who are deaf or hard of hearing, covert communications, or even underwater communications. With their high sensitivity to vibrations and matched impedance with the skin, the fabrics are particularly suited for physiological sensing. Heart auscultation is a fundamental tool in the diagnosis of cardiovascular diseases and abnormalities. Figure 5h shows that an acoustic shirt contacting the chest of a person efficiently captures cardiac signals (Fig. 5i), acting as a skin-interfaced stethoscope. The signal, with a signal-to-noise ratio as high as 30 dB, surpasses that of recent thin-film acoustic devices[28,29] and conveys useful information about the wearer's cardiovascular system. The resting heart rate was measured to be 70 beats per min. The shirt also clearly detects the louder S1 sound and the weaker S2 sound (Fig. 5i). Notably, the fibre captures the splitting of S1 as well as the splitting of S2 (Supplementary Fig. 30), previously unachievable with thin-film devices[28,29]. Supplementary Audio 1 presents high-quality heart sounds recorded using the acoustic shirt. The ability to detect the mechanical action of the heart using the fabric may enable wearers to monitor their heart and respiratory condition in a comfortable, continuous, real-time and long-term manner.

In summary, we have described the principles, materials, and mechanisms leading to the realization of an acoustic fabric. The resulting fabrics are capable of efficiently detecting audible sounds with performance on par with commercial microphones. Applications in sound-direction detection, acoustic communications, and heart-sound auscultation illustrate the wide-ranging applicability of this technology to enable advances in fabric-based human–computer interfaces[30], physiological monitoring and health care[31], aerospace engineering[32], communications[33], biomedicine[34], robotics[35] and computing fabrics.

Online content

Any methods, additional references, Nature Research reporting summaries, source data, extended data, supplementary information, acknowledgements, peer review information; details of author contributions and competing interests; and statements of data and code availability are available at https://doi.org/10.1038/s41586-022-04476-9.

1. Delany, M. E. & Bazley, E. N. Acoustical properties of fibrous absorbent materials. *Appl. Acoust.* **3**, 105–116 (1970).
2. Tang, X. & Yan, X. Acoustic energy absorption properties of fibrous materials: A review. *Compos. Part A* **101**, 360–380 (2017).
3. Kozlov, A. S., Baumgart, J., Risler, T., Versteegh, C. P. C. & Hudspeth, A. J. Forces between clustered stereocilia minimize friction in the ear on a subnanometre scale. *Nature* **474**, 376–379 (2011).
4. Shi, J. et al. Smart textile-integrated microelectronic systems for wearable applications. *Adv. Mater.* **32**, 1901958 (2019).
5. Abouraddy, A. F. et al. Towards multimaterial multifunctional fibres that see, hear, sense and communicate. *Nat. Mater.* **6**, 336–347 (2007).

6. Yan, W. et al. Thermally drawn advanced functional fibers: new frontier of flexible electronics. *Mater. Today* **35**, 168–194 (2020).
7. Weng, W. et al. A route toward smart system integration: from fiber design to device construction. *Adv. Mater.* **32**, 1902301 (2020).
8. Chen, G., Li, Y., Bick, M. & Chen, J. Smart textiles for electricity generation. *Chem. Rev.* **120**, 3668–3720 (2020).
9. Khudiyev, T. et al. 100-m-long thermally drawn supercapacitor fibers with applications to 3D printing and textiles. *Adv. Mater.* **32**, 2004971 (2020).
10. Rein, M. et al. Diode fibres for fabric-based optical communications. *Nature* **560**, 214–218 (2018).
11. Zhang, X. A. et al. Dynamic gating of infrared radiation in a textile. *Science* **363**, 619–623 (2019).
12. Hsu, P. C. et al. Radiative human body cooling by nanoporous polyethylene textile. *Science* **353**, 1019–1023 (2016).
13. Zhu, B. et al. Subambient daytime radiative cooling textile based on nanoprocessed silk. *Nat. Nanotechnol.* **16**, 1342–1348 (2021).
14. Shi, X. et al. Large-area display textiles integrated with functional systems. *Nature* **591**, 240–245 (2021).
15. Loke, G. et al. Digital electronics in fibres enable fabric-based machine-learning inference. *Nat. Commun.* **12**, 3317 (2021).
16. Egusa, S. et al. Multimaterial piezoelectric fibres. *Nat. Mater.* **9**, 643–648 (2010).
17. Chocat, N. et al. Piezoelectric fibers for conformal acoustics. *Adv. Mater.* **24**, 5327–5332 (2012).
18. Fay, J. P., Puria, S. & Steele, C. R. The discordant eardrum. *Proc. Natl Acad. Sci. USA* **103**, 19743–19748 (2006).
19. Qu, Y. et al. Superelastic multimaterial electronic and photonic fibers and devices via thermal drawing. *Adv. Mater.* **30**, 1707251 (2018).
20. Acosta, M. et al. BaTiO$_3$-based piezoelectrics: fundamentals, current status, and perspectives. *Appl. Phys. Rev.* **4**, 041305 (2017).
21. Setiadi, D., Binnie, T. D., Regtien, P. & Wübbenhorst, M. Poling of VDF/TrFE copolymers using a step-wise method. In *9th Int. Symp. Electrets (ISE)* (eds Xia, Z. & Zhang, H.) 831–835 (IEEE, 1996).
22. Zhang, Y., Bowen, C. R. & Deville, S. Ice-templated poly(vinylidene fluoride) ferroelectrets. *Soft Matter* **15**, 825–832 (2019).
23. Safari, A. & Akdoğan, E. K. (eds) *Piezoelectric and Acoustic Materials for Transducer Applications* (Springer, 2008).
24. Lang, C., Fang, J., Shao, H., Ding, X. & Lin, T. High-sensitivity acoustic sensors from nanofibre webs. *Nat. Commun.* **7**, 11108 (2016).
25. Kang, S. et al. Transparent and conductive nanomembranes with orthogonal silver nanowire arrays for skin-attachable loudspeakers and microphones. *Sci. Adv.* **4**, eaas8772 (2018).
26. Khan, A., Abas, Z., Soo Kim, H. & Oh, I. K. Piezoelectric thin films: an integrated review of transducers and energy harvesting. *Smart Mater. Struct.* **25**, 053002 (2016).
27. Kinsler, L., Frey, A., Coppens, A. & Sanders, J. *Fundamentals of Acoustics* 4th edn (Wiley, 2000).
28. Yang, Y. & Gao, W. Wearable and flexible electronics for continuous molecular monitoring. *Chem. Soc. Rev.* **48**, 1465–1491 (2019).
29. Xiong, J., Chen, J. & Lee, P. S. Functional fibers and fabrics for soft robotics, wearables, and human–robot interface. *Adv. Mater.* **33**, 2002640 (2021).
30. Loke, G. et al. Computing fabrics. *Matter* **2**, 786–788 (2020).
31. Wang, W., Yu, A., Zhai, J. & Wang, Z. L. Recent progress of functional fiber and textile triboelectric nanogenerators: towards electricity power generation and intelligent sensing. *Adv. Fiber Mater.* **3**, 394–412 (2021).
32. Ahmed, A., Hossain, M. M., Adak, B. & Mukhopadhyay, S. Recent advances in 2D MXene integrated smart-textile interfaces for multifunctional applications. *Chem. Mater.* **32**, 10296–10320 (2020).
33. Cummer, S. A., Christensen, J. & Alù, A. Controlling sound with acoustic metamaterials. *Nat. Rev. Mater.* **1**, 16001 (2016).
34. Han, M. et al. Three-dimensional piezoelectric polymer microsystems for vibrational energy harvesting, robotic interfaces and biomedical implants. *Nat. Electron.* **2**, 26–35 (2019).
35. Yang, G.-Z. et al. The grand challenges of *Science Robotics*. *Sci. Rob.* **3**, eaar7650 (2018).

Article

Methods

Preparation of nanostructured piezoelectric composites

Poly(vinylidene fluoride-co-trifluoroethylene) (PVDF-TrFe, Piezotech FC 30) with 30 mol% TrFe was dissolved in dimethylformamide (DMF) (1:10, w:w) by continuous stirring for 5 h. Barium titanate particles (spherical, 99.9%, 200 nm, tetragonal phase, US Research Nanomaterials; average diameter of 260 nm as shown in Supplementary Fig. 32) were added and stirred for 12 h to form a suspension. The ratio of BaTiO$_3$ to PVDF-TrFE is 1:5 by weight. The suspension was sonicated for 2 h, changing the water every 15 min to prevent it from warming up. The suspension was stirred again for 20 h and then sonicated for 3 h, changing the water every 15 min. It was then mixed in a centrifugal mixer at 3,500 r.p.m. for 10 min. The mixture was poured onto a glass substrate to form a film as the DMF evaporates. After drying at room temperature for one day, the composite separates from the solvent and forms a film at the bottom of the dish with the DMF solvent on top. The film is removed from the DMF and dried in a 60 °C oven for five days before use.

Preform fabrication and thermal drawing

The acoustic fibre was drawn from a macroscopic rectangular preform with dimensions of 2.5 cm × 1.38 cm × 18 cm. A hot press was used to press the piezocomposite, CPE (ET331080, Goodfellow), and SEBS (grade G1657 from Kraton Performance Polymers) layers into sheets of the appropriate thickness. All the materials were then cut and assembled into a mould according to the fibre architecture. The SEBS cladding, CPE electrodes (1.4 mm thick), and piezoelectric composite layer (600 μm) were consolidated using a hot press at 100 °C. The preform was drawn in a three-zone vertical tube furnace with a top-zone temperature of 120 °C, a middle-zone temperature of 252 °C, and a bottom-zone temperature of 80 °C. CPE is a typical conductive thermoplastic polymeric electrode used in thermally drawn fibres. Compared to SEBS, CPE exhibits a lower viscosity and thereby undergoes a stable flow. On the other hand, its viscosity is higher than that of the piezocomposite, which delays the onset of capillary instability of the molten piezocomposite during the draw. CPE exhibits a conductivity of ~2 S m^{-1}, enabling transverse electronic transport. During the drawing process, 50-μm copper microwires (50 μm, Goodfellow) with a conductivity of ~10^7 S m^{-1} do not undergo thermoplastic deformation but are fed into two empty channels in the CPE, and this convergence technique results in fibres containing four wires that are fully embedded in the CPE layers, leading to axial electron transport along the fibre length. The fibre dimensions are monitored with laser micrometers and the cross-section dimensions of the fibre are scaled down 20× compared to those of the preform. A detailed protocol of the acoustic fibre design and fabrication is elaborated in Supplementary Note 1.

The oscillatory shear rheology characterization

The oscillatory shear rheology characterization was carried out on a rheometer (AR 2000, TA Instruments). For rheological characterization, the polymer plates (1,500 μm thick) were heated from 50 to 220 °C at 1 °C min^{-1}. The test was done in the oscillatory mode with an angular frequency of 1 rad s^{-1} and an oscillation strain of 1%.

X-ray diffraction characterization

Wide-angle and small-angle X-ray scattering characterizations were performed at the Massachusetts Institute of Technology (MIT) Center for Materials Science and Engineering (CMSE) X-ray Diffraction Shared Experimental Facility on a SAXSLAB system. Cu Kα1 X-rays of wavelength 1.5409 Å were produced by the microfocus X-ray source (002, Rigaku). Osmic staggered parabolic multilayer optics focused the beam crossover at the second pinhole. Two sets of jaw collimation slits (JJ X-ray) with diameters of 0.45 mm and 0.2 mm, respectively, were used to define the beam. The system was calibrated using silver behenate as

a standard. The piezocomposite samples harvested from the fibre were directly fixed on the holes of the standard sample plate of the facility.

Piezoelectric charge coefficient d_{31} measurement

Rectangular gold (10 nm) electrodes were coated on both sides of the sample, using a sputter coater (Q300TD, Quorum Technologies, UK). The electrode length and width were measured using an optical microscope. The d_{31} measurement set-up is shown in Supplementary Fig. 6. The d_{31} values with different dynamic stress values were measured by manually applying and removing a weight (~1–200 g) at the end of the fibre. A quartz force sensor (208C01, PCB Piezotronics, USA) was used to monitor the force applied on the fibre. A preforce of 10 g (0.098 N) was applied to keep the strain in the vertical direction. The generated charge was monitored using a electrometer (617, Keithley, USA). Through a data-acquisition card (NI USB-6002, National Instruments, USA), the whole system was operated by the LabView software.

3D acoustical-mechano-electro model

A 3D acoustical-mechano-electro model (COMSOL Multiphysics) that couples acoustics, mechanics and electrostatics was developed to simulate the system. The validity of the model is demonstrated in Supplementary Note 8. All the components of the fibre were included in the model, and the materials properties are summarized in Supplementary Table 1.

In the 3D simulation, the membrane was modelled with a two-dimensional shell module because the membrane thickness is much smaller than the lateral size (8 cm × 8 cm). A 6.5-cm-long fibre containing the piezoelectric domain and electrodes was placed on the membrane surface at the centre. The whole structure was placed in an air domain with perfect matching boundary layers in the surroundings. A pre-defined background acoustic plane wave was perpendicularly incident onto the membrane side with the fibre and induced vibration in the fibre and the membrane. The vibration was converted to voltage variation by the piezoelectric material in the fibre. Four physics modules were applied to compute the relevant physical effects: the pressure acoustic module for the air domain, the shell module for the membrane, the solid mechanics module for the fibre, and the electrostatics module for the piezoelectric material and electrodes.

The type and size of the mesh varied on different parts of the model. The air background and the shell model of the membrane were meshed with free tetrahedral and triangular elements, respectively. The fibre was meshed by sweeping the transversal surface, which was meshed with free triangular elements, along the fibre axis. The maximum size of the elements was determined by iteratively reducing the maximum mesh size in simulations until the change in the output values of interest between two consecutive simulations was below 5% (Supplementary Table 2).

The output of the simulation included the voltage from the electrodes, stress, displacement and acoustic pressure at various locations of the model. The simulation allowed us to vary the system settings computationally and conduct sensitivity analyses for various parameters.

Acoustic and laser vibrometry characterization

In all cases, samples fixed in a frame (see detailed methods in Supplementary Note 5) were placed 2 m from the speaker. A signal generator was used to input the desired frequency and power to the speaker. A decibel meter was placed to the side of the frame, in the same plane as the fibre, and the power of the signal generator was adjusted until the desired sound pressure level was reached. The fibre was connected to a printed circuit board, which was connected to an oscilloscope that recorded the response of the fibre. The sample holder (that is, the frame) was placed on 10 cm of acoustic-insulating foam on the floor of an acoustic studio. The speaker also was set on foam on the floor. The displacement and vibrational modal patterns of the

fibre-on-membrane and the acoustic fabric in response to different frequencies was concurrently measured using a scanning vibrometer (PSV-500, Polytec, USA) while measuring the output voltage from the samples. Fast Fourier transforms were performed on each voltage signal to determine the output voltage. All characterization was performed in an acoustically damped and isolated music practice room, as an approximation to an anechoic chamber.

Standalone fibre. The two ends of the 6.7-cm fibre were attached across from each other in a 6.7 cm × 6.7 cm aluminium frame clamped to stand in an upright position.

Fibre on Mylar. The Mylar (50 μm in thickness, 8 cm in length and 8 cm in width; ES301955, metallized on one side, Goodfellow, UK) was fastened in a square 8-cm aluminium frame clamped in the upright position. A metallized Mylar can more efficiently reflect the visible light and generate higher signal-to-noise ratio data during the laser vibrometer measurements. The boundary condition was well controlled (see detailed methods in Supplementary Note 5). The 6.7-cm acoustic fibre was placed on the Mylar membrane. The SEBS cladding exhibits sufficient adhesion to the Mylar membrane that the fibre sticks to the membrane without any adhesive. The entire fibre was in contact with the Mylar membrane as the SEBS cladding of the fibre is sticky.

Acoustic woven fabrics. The acoustic fibre was woven into the fabric. For the acoustic characterization shown in Fig. 4, each fabric was clamped with well controlled boundaries conditions (see detailed methods in Supplementary Note 5). The fibre was ~6.7 cm long. The fabric size was 8 cm × 8 cm. The fabrics used for the demonstrations shown in Fig. 5 were integrated into shirts, so all fabrics were in a flexurally slack draped condition.

Weaving of acoustic fabrics
All fabrics were woven by hand on an eight-harness loom. A thin 100% cotton yarn (approximately 500 dtex, or 500 g per 10,000 m of yarn) was used for the warp. The warp density was 70 yarns per inch.

Two versions of a fabric were woven. The Twaron/cotton fabric used four strands of 405-dtex Twaron yarn (2200, 1210 linear density, Teijin Aramid, the Netherlands) as the weft, with a weft density of 48 yarns per inch. The pure cotton fabric used four strands of 500-dtex cotton yarn as the weft, with a weft density of 44 yarns per inch. This slightly lower weft density was used to match the weight of the first fabric as closely as possible.

The weave structure of these fabrics is a variation of plainweave. Plainweave is the simplest weave structure, in which warp yarns are alternately raised over and lowered under each weft yarn. In this variation, an extra warp yarn is added next to every sixth yarn in the warp sequence. When weaving the fabric, these two yarns act as a pair, always raising or lowering together. When inserting the acoustic fibre, one yarn in the pair is raised and the other is lowered. This results in a series of warp yarns covering the fibre, spaced 2.5 mm apart, whereas the fabric under the fibre is woven in plainweave without extra warp yarns. This method produces very similar weave structures in the main fabric and at the fibre location. The dimension of the fabric shown in Fig. 4 is 8 cm × 8 cm × 0.46 mm (length × width × thickness, l × w × t).

Warp yarns on a loom are always under tension. When weaving the acoustic fibre into the fabric, the tension of the covering warp yarns was controlled so that the warp yarns slightly compressed the acoustic fibre while securing its position. The optimized compression force was measured to be 0.0046 N. Two different methods were applicable for this purpose. For method 1, a group of yarns was inserted as a temporary weft in the same shed (configuration of raised warp yarns) as the fibre. These temporary wefts act as spacers between the warp yarns and the acoustic fibre: when they are removed from the fabric, the tension on these warp yarns is decreased. The second method of controlling

warp yarn tension is on looms with two warp beams. Warp yarns are separated into two groups when preparing the loom for weaving, and each group is wound onto one beam. The tension on each group of yarns can be controlled independently by rotating the beam, which is held in place by a brake wheel.

We note that a high compression force on the acoustic fibre impedes the ability of the fibre to bend and the synergistically coupled vibration between the fabric and the fibre, resulting in lower performance (Supplementary Fig. 29).

Additional fabrics were woven and integrated into shirts shown in Fig. 5. These fabrics use the same cotton-warp yarns and Twaron-weft yarns, and a similar modified plainweave structure in which an extra warp yarn is added after every third yarn. The same method of controlling warp tension when weaving the acoustic fibre was used.

The dimension of the acoustic shirt (Twaron weft/cotton warp) shown in Supplementary Video 2 is 36 cm × 23 cm × 0.46 mm (l × w × t). The dimension of the woven fibre is 6.7 cm × 0.1 cm × 0.69 mm (l × w × t). Thus, the volume fraction of the fibre occupying the fabric is only 0.097%.

Machine-wash test
The fibres and the fabrics were placed in a protective delicate laundry bag and washed with a portable mini washing machine (PUCWM11, PYLE). They experienced ten washing cycles, and each cycle was 15 min ('cotton' wash mode) at room temperature. No detergent was used during machine washing.

Ethics declaration
We have complied with all relevant ethical regulations.

Data availability
All data supporting the findings of this study are available within the article and its Extended Data and Supplementary Information. Representative source data for figures (Figs. 2h, 3, 4, 5g, i, Extended Data Figs. 1c, 2–5, 6c, 7b, 8 and Supplementary Figs. 13, 17) are publicly available at https://doi.org/10.5281/zenodo.5753073. Additional data are available from the corresponding authors upon reasonable request. Source data are provided with this paper.

36. Huang, Y. et al. Enhanced piezoelectricity from highly polarizable oriented amorphous fractions in biaxially oriented poly(vinylidene fluoride) with pure β crystals. *Nat. Commun.* **12**, 675 (2021).
37. Wang, K., Godfroid, T., Robert, D. & Preumont, A. Adaptive shell spherical reflector actuated with PVDF-TrFe thin film strain actuators. *Actuators* **10**, 7 (2021).
38. Wang, K., Alaluf, D., Rodrigues, G. & Preumont, A. Precision shape control of ultra-thin shells with strain actuators. *J. Appl. Comput. Mech.* **7**, 1130–1137 (2021).
39. Guo, S., Duan, X., Xie, M., Aw, K. C. & Xue, Q. Composites, fabrication and application of polyvinylidene fluoride for flexible electromechanical devices: a review. *Micromachines* **11**, 1076 (2020).
40. Kim, H., Fernando, T., Li, M., Lin, Y. & Tseng, T. L. B. Fabrication and characterization of 3D printed BaTiO₃/PVDF nanocomposites. *J. Compos. Mater.* **52**, 197–206 (2018).
41. Kim, H. et al. Increased piezoelectric response in functional nanocomposites through multiwall carbon nanotube interface and fused-deposition modeling three-dimensional printing. *MRS Commun.* **7**, 960–966 (2017).
42. Bodkhe, S., Turcot, G., Gosselin, F. P. & Therriault, D. One-step solvent evaporation-assisted 3D printing of piezoelectric PVDF nanocomposite structures. *ACS Appl. Mater. Interfaces* **9**, 20833–20842 (2017).
43. Pi, Z., Zhang, J., Wen, C., Zhang, Z.-b & Wu, D. Flexible piezoelectric nanogenerator made of poly(vinylidenefluoride-co-trifluoroethylene) (PVDF-TrFE) thin film. *Nano Energy* **7**, 33–41 (2014).
44. Baur, C. et al. Enhanced piezoelectric performance from carbon fluoropolymer nanocomposites. *J. Appl. Phys.* **112**, 124104 (2012).
45. Zeng, R., Kwok, K. W., Chan, H. L. W. & Choy, C. L. Longitudinal and transverse piezoelectric coefficients of lead zirconate titanate/vinylidene fluoride-trifluoroethylene composites with different polarization states. *J. Appl. Phys.* **92**, 2674–2679 (2002).
46. Omote, K., Ohigashi, H. & Koga, K. Temperature dependence of elastic, dielectric, and piezoelectric properties of "single crystalline" films of vinylidene fluoride trifluoroethylene copolymer. *J. Appl. Phys.* **81**, 2760–2769 (1997).
47. Wang, H., Zhang, Q. M., Cross, L. E. & Sykes, A. O. Piezoelectric, dielectric, and elastic properties of poly(vinylidene fluoride/trifluoroethylene). *J. Appl. Phys.* **74**, 3394–3398 (1993).

Article

**Extended Data Fig. 1 | Piezocomposite preparation and characterization.** **a**, Schematic of the fabrication flow of the piezocomposite. The detailed description is shown in Methods. The nanoparticles must be homogeneously distributed in the P(VDF-TrFE) matrix as aggregation can deteriorate energy conversion and causes fibre breakage during the draw. This requirement is achieved by using a planetary centrifugal mixing process that applies ultrastrong shearing forces to the composite suspension. **b**, SEM micrograph of a piezocomposite thin film fabricated without centrifuging treatment (left) and with centrifuging treatment (right). The inset in the left image highlights a severe agglomeration of $BaTiO_3$ nanoparticles, whereas the inset in the right image presents a homogenous distribution of nanoparticles. **c**, Wide-angle X-ray scattering characterization of the hot-pressed as-cast composite and

drawn P(VDF-TrFE)/$BaTiO_3$ fibre showing the β phase of P(VDF-TrFE) and tetragonal phase of the $BaTiO_3$ nanoparticles. The sharp equatorial arcs in the diffraction pattern of the drawn sample demonstrates that the thermal drawing process aligns the polymer chains along the draw direction. DD, fibre-drawing direction; TD, fibre transverse direction. **d**, Bright-field TEM image of the $BaTiO_3$ nanoparticles harvested from the fibre. The inset shows the selected-area electron diffraction pattern from transmission electron microscopy (TEM) characterization of a $BaTiO_3$ nanoparticle. Each nanoparticle is monocrystalline in the tetragonal phase. The particle size distribution is shown in Supplementary Fig. 32. The TEM diffraction was performed using an FEI Tecni (G2 Spirit TWIN) under 120 kV.

Article

a

b
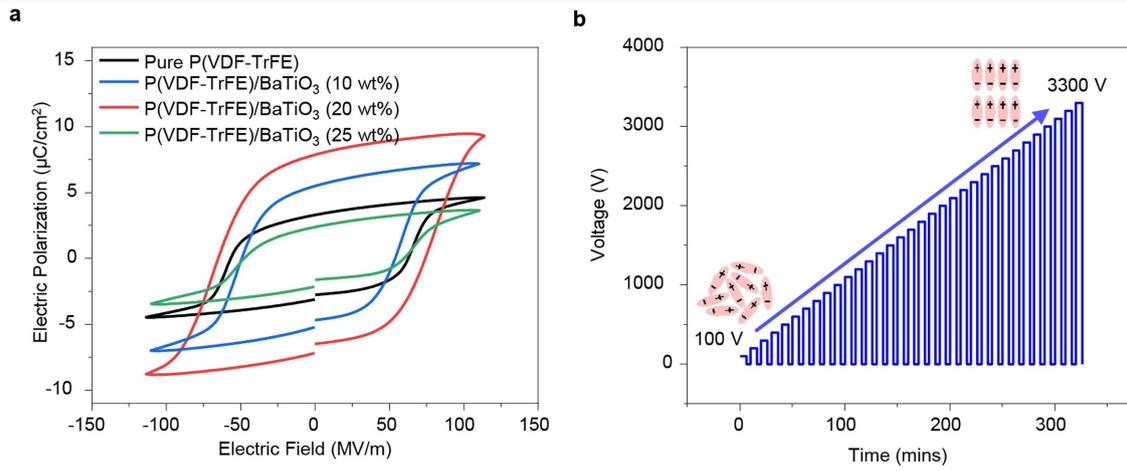
Extended Data Fig. 2 | Hysteresis loops and poling method of the fibre. a, Electric polarization versus electric field hysteresis loops of a pure P(VDF-TrFE) fibre and fibres with varying weight percentages of BaTiO$_3$ nanoparticles (10, 20, 25 wt%). **b**, Stepwise poling method. The poling voltage is increased to 3,300 V in 100-V steps. The schematics show the dipole orientation before and after the poling process.
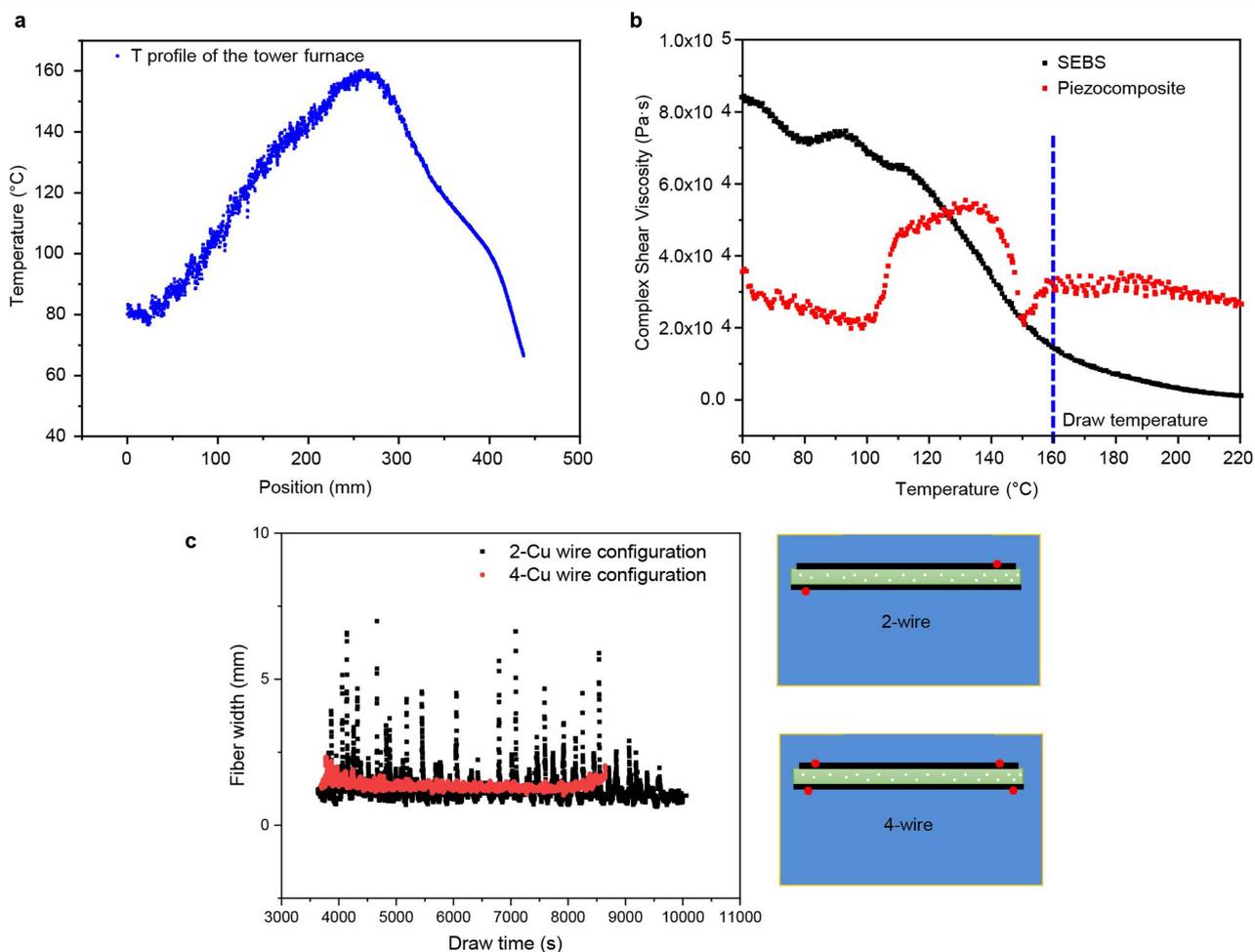
**Extended Data Fig. 3 | Optimization of the fibre design and fabrication.**
a, Temperature profile of the tower furnace. The draw temperature at the neck-down region is around 160 °C. The top surface of the furnace in the fibre draw tower was set to be the zero position. **b**, Rheological properties of the SEBS and piezocomposite. The oscillatory shear rheology of SEBS is slightly lower than that of the piezocomposite at the draw temperature. Thus, to ensure a smooth flow of the molten piezocomposite, two Cu wires instead of one wire are embedded in each of the two CPE electrodes. The tension applied on the four wires during the draw exerts compressive stress onto the molten piezocomposite in the neck-down region, thus preventing capillary breakup of the piezocomposite and creating highly uniform fibres (Extended Data Fig. 3c). **c**, Characterization of the fibre size for two different configurations. The 4-Cu wire configuration leads to a highly uniform fibre, whereas the fibre size in the 2-Cu wire configuration fluctuates a lot because of the fluid instability.

a

b
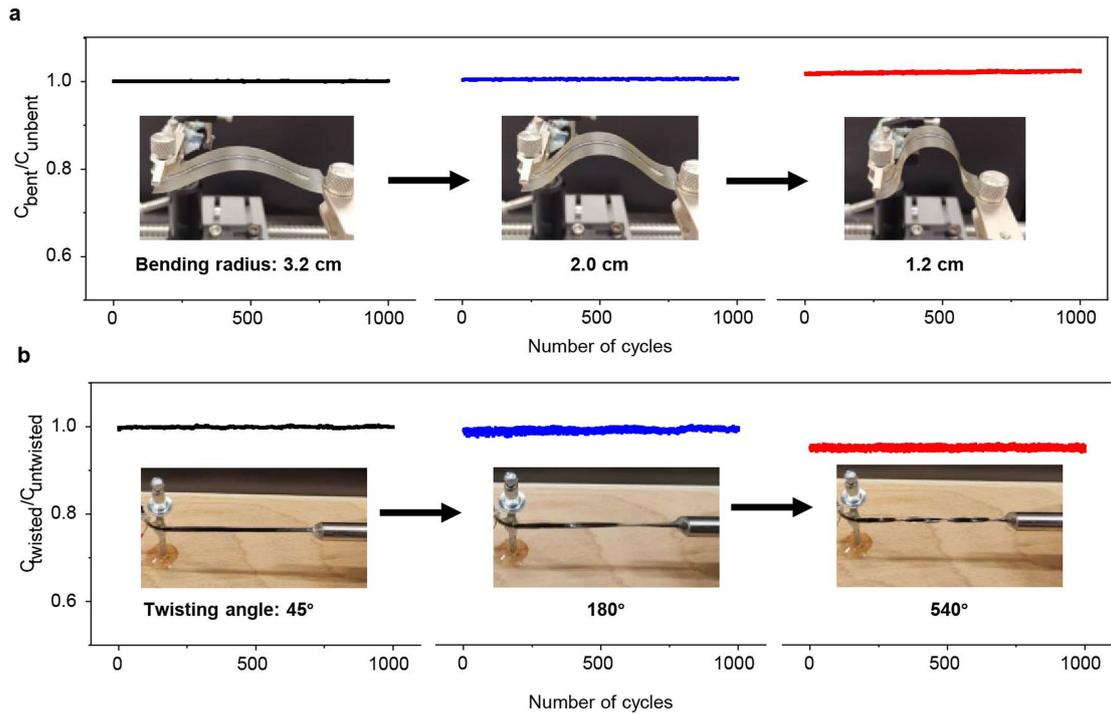
Extended Data Fig. 4 | Stability of the electric property of the fibre. a, The ratio of the capacitance (*C*) after and before the fibre was bent with, from right to left, bending radii of 3.2, 2.0 and 1.2 cm for 1,000 cycles. To ensure a reliable bending radius, the fibre was mounted on a polymer substrate. After the first 1,000-cycle test, the fibre was successively subject to the second and the third 1,000-cycle tests. **b**, The ratio of the capacitance after and before the fibre was twisted with, from right to left, angles of 45°, 180° and 540° for 1,000 cycles. All tests were done successively.
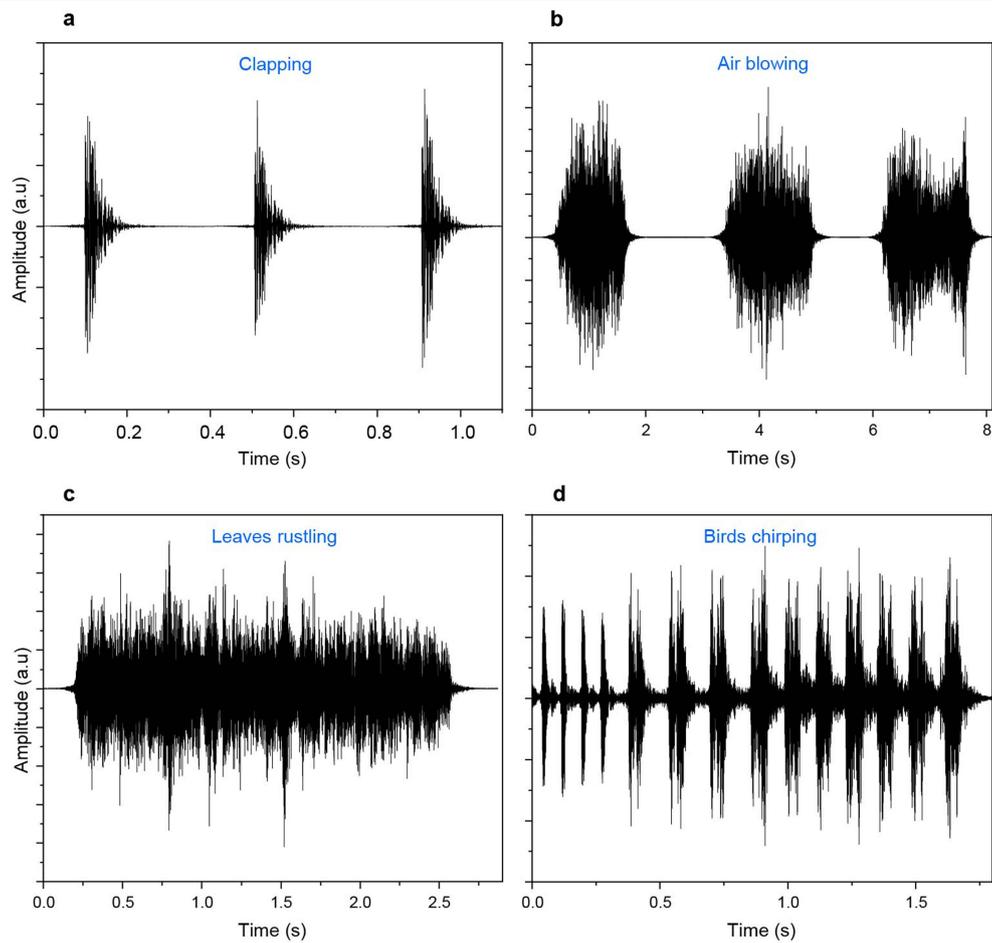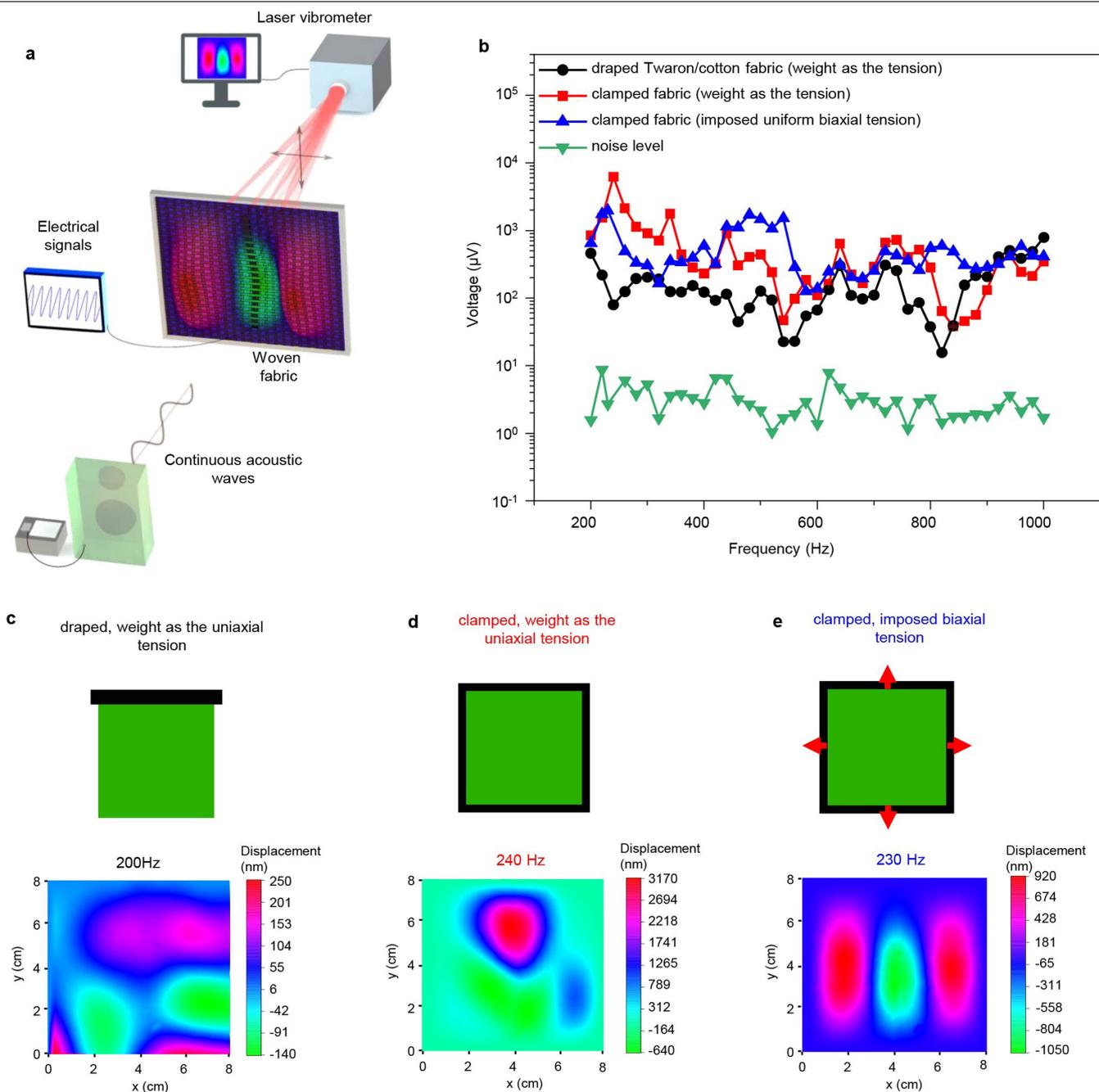
Extended Data Fig. 5 | Audible sound detection using the fibre-on-membrane. a–d, Time-dependent waveforms of a clap (**a**), air blowing (**b**), leaves rustling (**c**) and birds chirping (**d**), detected using the fibre-on-membrane system.
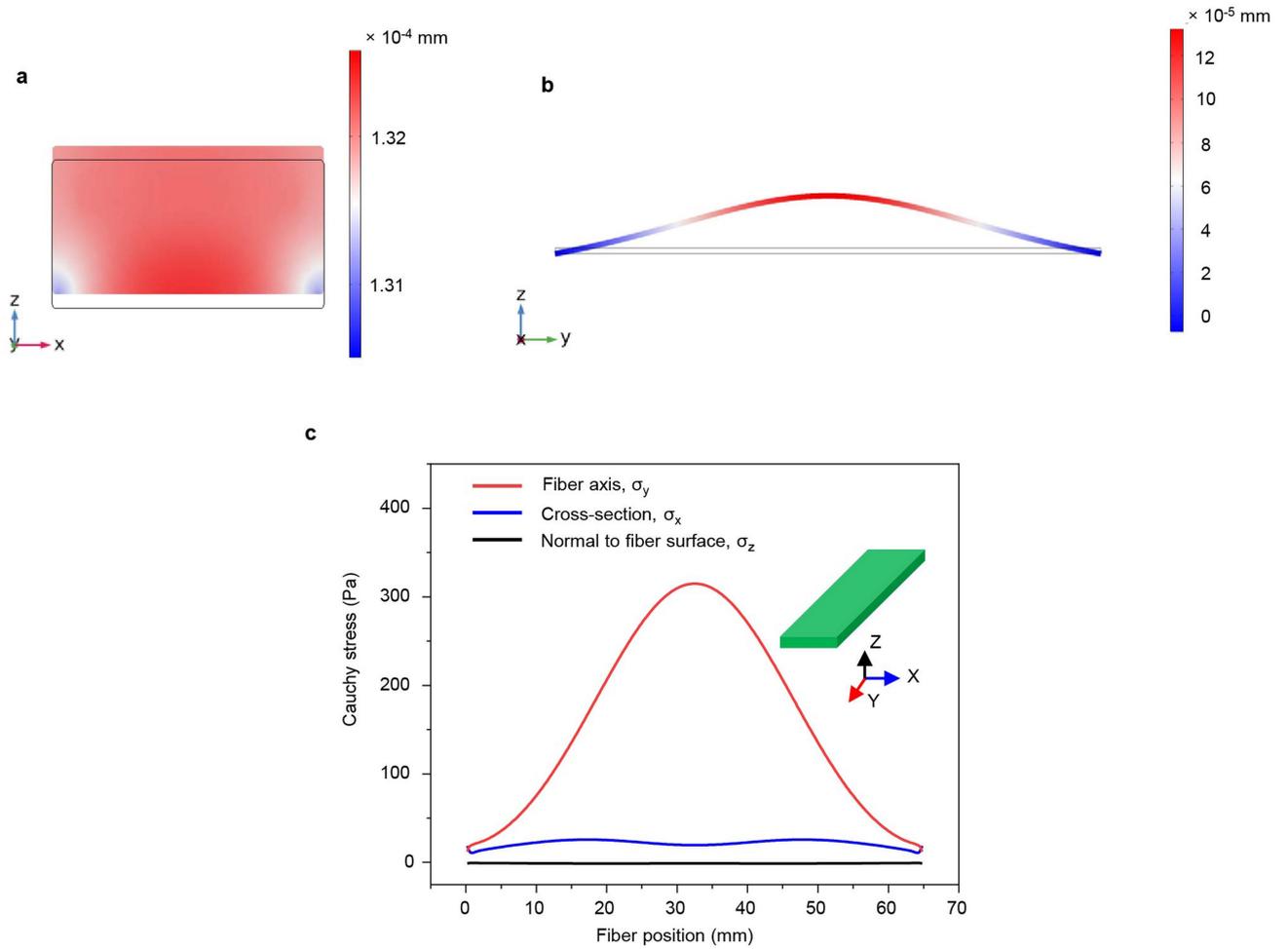
Extended Data Fig. 6 | Stress and bending analysis of the fibre-on-Mylar. **a**, The bending/displacement of the middle *x* plane of the fibre at 300 Hz (the deformation is scaled by a factor of 500) **b**, The bending/displacement of the middle *y* plane of the fibre (the deformation is scaled by a factor of 50,000). **c**, The Cauchy stress distribution of the line in the middle of the piezocomposite along the fibre length. All simulation results were obtained from the 3D COMSOL model.

a, Laser vibrometer

Electrical signals

Woven fabric

Continuous acoustic waves

b

- draped Twaron/cotton fabric (weight as the tension)
- clamped fabric (weight as the tension)
- clamped fabric (imposed uniform biaxial tension)
- noise level

Voltage (μV) vs Frequency (Hz)

c draped, weight as the uniaxial tension

200Hz — Displacement (nm): 250, 201, 153, 104, 55, 6, -42, -91, -140

d clamped, weight as the uniaxial tension

240 Hz — Displacement (nm): 3170, 2694, 2218, 1741, 1265, 789, 312, -164, -640

e clamped, imposed biaxial tension

230 Hz — Displacement (nm): 920, 674, 428, 181, -65, -311, -558, -804, -1050

Extended Data Fig. 7 | Performance and modal patterns comparison between three fabrics where the piezoelectric fibre was woven directly.
**a**, The set-up used for the concurrent measurements. **b**, The frequency response and modal patterns of fabrics for three boundary conditions and tensions: **c**, A draping fabric with the top edge clamped where tension is supplied only by the fabric weight uniaxially. **d**, A fully clamped fabric where the only tension is supplied by fabric weight uniaxially. **e**, A fully clamped fabric with externally imposed uniform biaxial tension. The uniform biaxial tension

was achieved using the method elaborated in Supplementary Note 5. These measurements clearly show excellent electrical signals at audible frequency from all fabrics well above the noise regardless of the specifics of tension or boundary conditions. These measurements clearly establish and substantiate not only that the fabric is sensitive under draping conditions but also that the electrical response emanates from nanometre-amplitude displacements in the fabric, which are captured by the fibre and are then transduced into electrical signals.
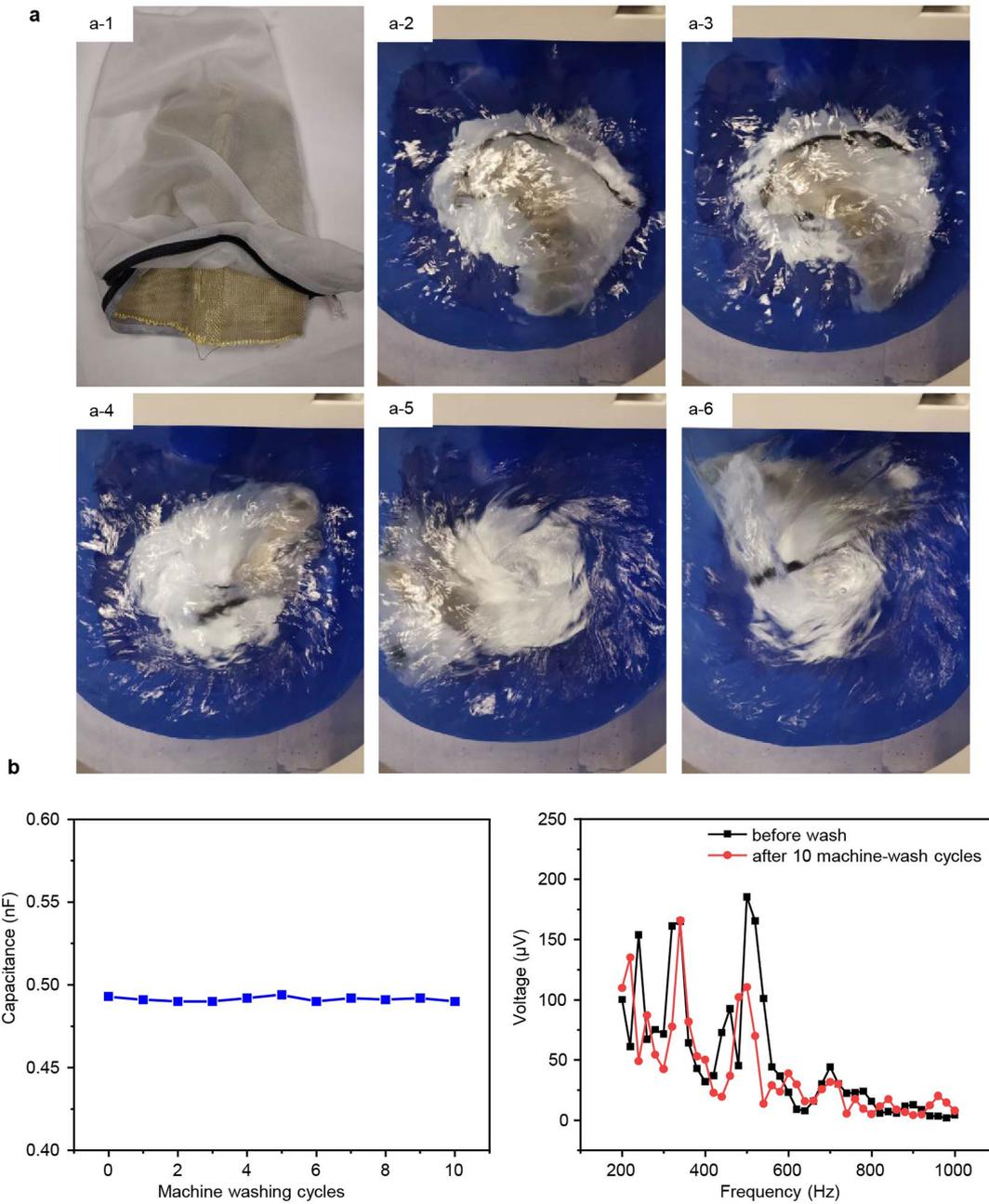
Extended Data Fig. 8 | The washability of the acoustic fabric. a, Snapshot photographs of the acoustic fabric being washed in a washing machine at room temperature. **b**, The constant capacitance with washing cycles (left); and the voltage versus frequency of the acoustic fabric before it is washed and after it is washed for ten cycles (right). Note that the cotton yarns in this fabric are grey, whereas the cotton yarns shown in Fig. 4 are green. The warp cotton yarn is a size 20/2 cotton with a set of 60 ends per inch and was threaded through a 12-dent reed. The weft yarn is a 1,210-dtex Twaron yarn (Tejin Aramid, The Netherlands). Four strands of Twaron yarn (strands were not twisted together) were used in the weft direction. The size of the fabric is 17 cm × 17 cm × 1 mm. The compression force the warp yarns applied to the fibre was measured to be 16.9 g using a force sensor (ZC-RP-C5ST-LF5-1024, Taidacent).
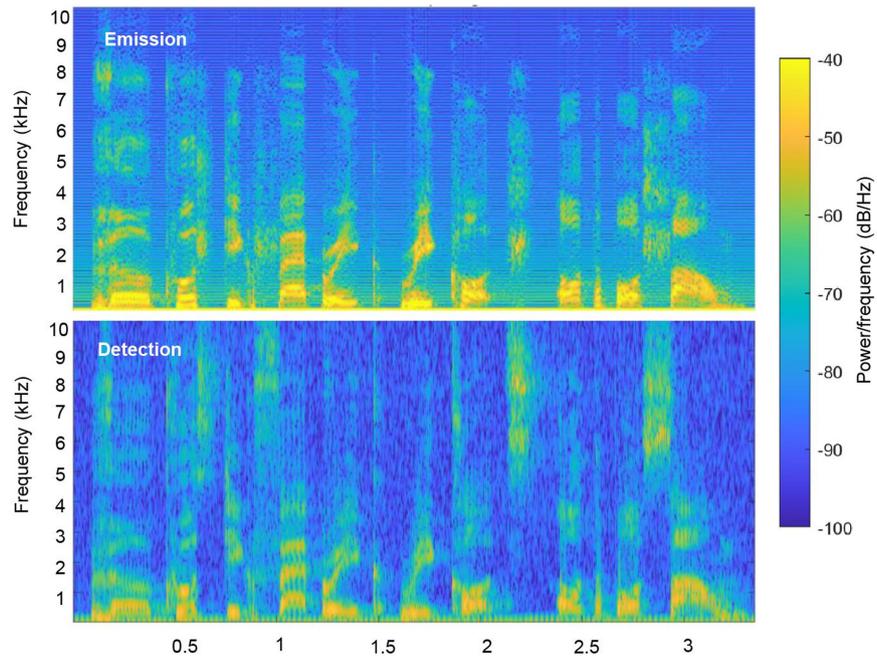
Extended Data Fig. 9 | Short-time Fourier transform spectrograms. The spectrograms of the audio used to drive the fabric emitter (top) and the audio detected by the fabric receiver (bottom) shown in Fig. 5g. Signals were sampled at 50 kHz, and data are shown from 20 Hz to 10 kHz in each case. A time window of 5 ms and overlap percentage of 20% were used to produce the spectrograms.

Article

Extended Data Table 1 | Comparison of direct d_{31} piezoelectric coefficient between thermally drawn P(VDF-TrFE)/BTO fibre and state-of-the-art PVDF-based materials

Materials	Direct d_{31} (pC/N)	References
P(VDF-TrFE) (70/30mol%)/BTO Thermally drawn	46	This work
Biaxially oriented PVDF Stretched	11-22	36
P(VDF-TrFE) Spray-coated	12-15	37
P(VDF-TrFE)	15	38
PVDF 3D printed	18	39
PVDF/BTO 3D printed	0.021	40
PVDF/BTO/carbon nanotubes 3D printed	0.13	41
PVDF/BTO 3D printed	18	42
P(VDF-TrFE) 75/25 mol% Spin-coated	25	43
PVDF/Buckminster fullerenes (C60) and SWCNTs Ultrasonication	32-65	44
P(VDF-TrFE) (75/25 mol%)/PZT Compressed	<8	45
P(VDF-TrFE) 75/25 mol% Stretched	7	46
P(VDF-TrFE) 75/25 mol%	10.7	47

Refs. [36–47].